Electronic Supplementary Material (ESI) for Journal of Materials Chemistry A.

Phase separation synthesis of trinickel monophosphide porous hollow nanospheres for efficient hydrogen evolution

Lihuang Jin,[a,b,c] Han Xia,[a,b,c] Zhipeng Huang,[a,b,c] Cuncai Lv,[a,b,c] Jie Wang,[a,b,c] Mark G. Humphrey,[d] and Chi Zhang[a,b,c]

[a.] *China-Australia Joint Research Center for Functional Materials, School of Chemistry Science and Engineering, Tongji University, Shanghai, 200092, China. Email: zphuang@tongji.edu.cn; chizhang@tongji.edu.cn.*

[b.] *Advanced Research Institute, Tongji University, Shanghai, 200092, China*

[c.] *Functional Molecular Materials Research Centre, Scientific Research Academy, China-Australia Joint Research Center for Functional Materials, Jiangsu University, Zhenjiang, 212013, China.*

[d.] *Research School of Chemistry, Australian National University, Canberra, ACT 2601, Australia.*

Electronic Supplementary Information

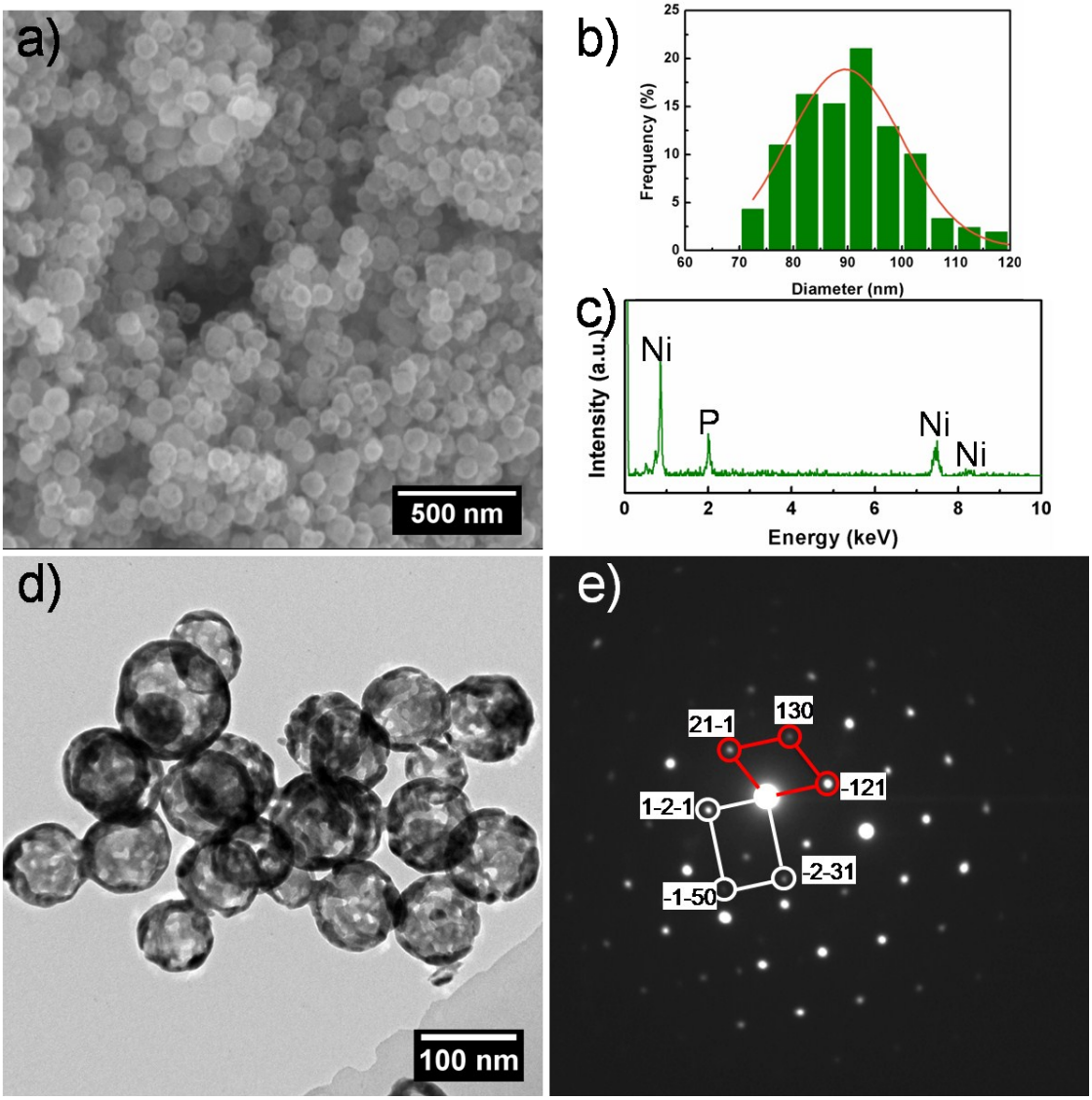

Figure S1. a) Low magnification SEM image of the Ni_3P PHNs. (b) Diameter distribution of the Ni_3P PHNs. The histogram shows the experimental results with a superimposed Gaussian curve-fitting. c) EDX spectrum of the Ni_3P PHNs. d) Low-magnification TEM image of the Ni_3P PHNs. e) SAED pattern recorded from a Ni_3P PHN. The red framework illustrates the lattice pattern of the [3-15] zone axis, and the white framework illustrates that of the [5-17] zone axis.

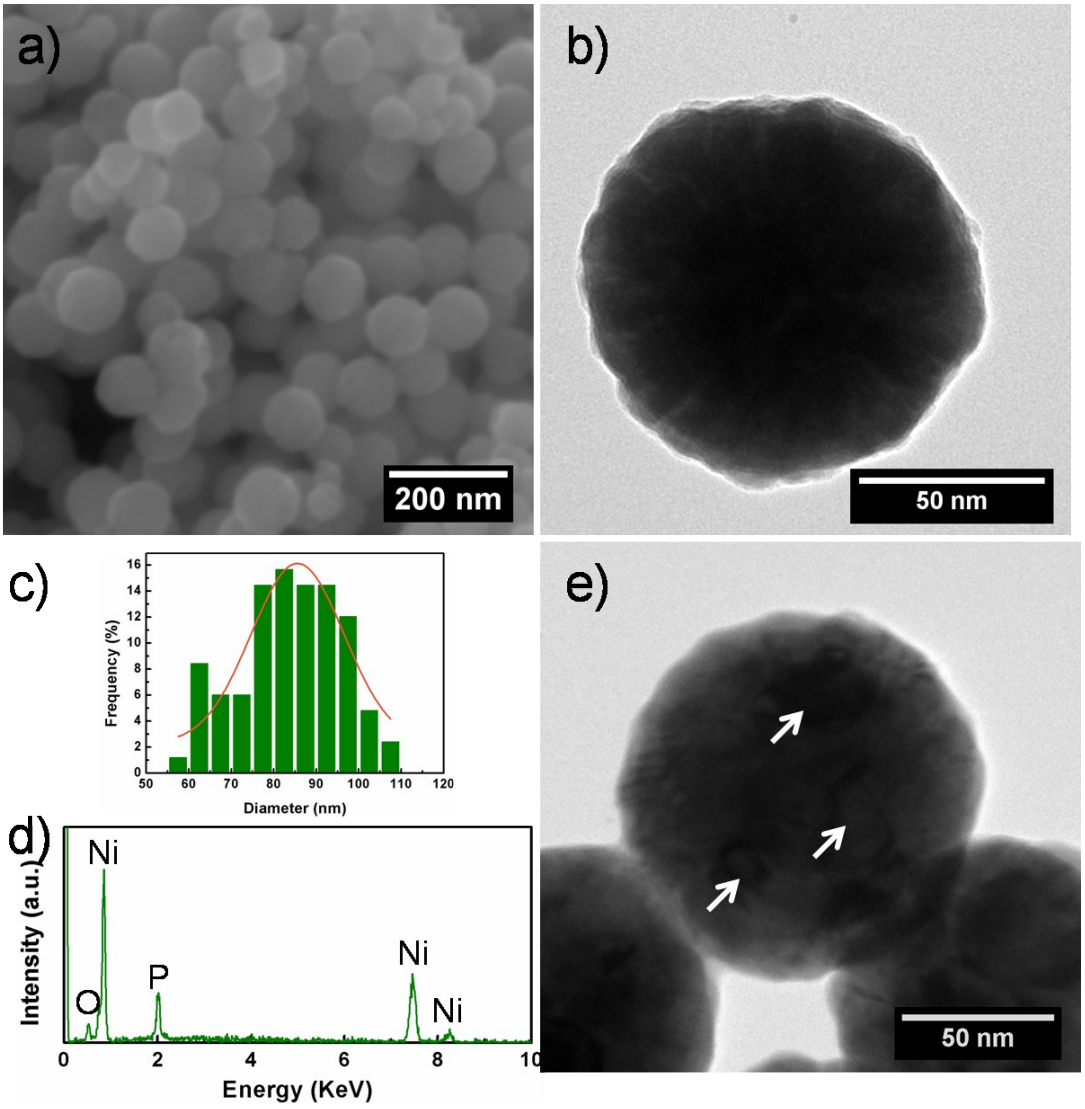

Figure S2. a) Low-magnification SEM image of amorphous Ni-P nanoparticles. b) TEM image of an amorphous Ni-P nanoparticle. c) Diameter distribution of the amorphous Ni-P nanoparticles. The histogram shows the experimental results with a superimposed Gaussian curve-fitting. d) EDX spectrum of the amorphous Ni-P nanoparticles. e) TEM image of an annealed Ni-P nanoparticle (500 ^{o}C, 1 h). The arrows in e) indicate the darker phase.

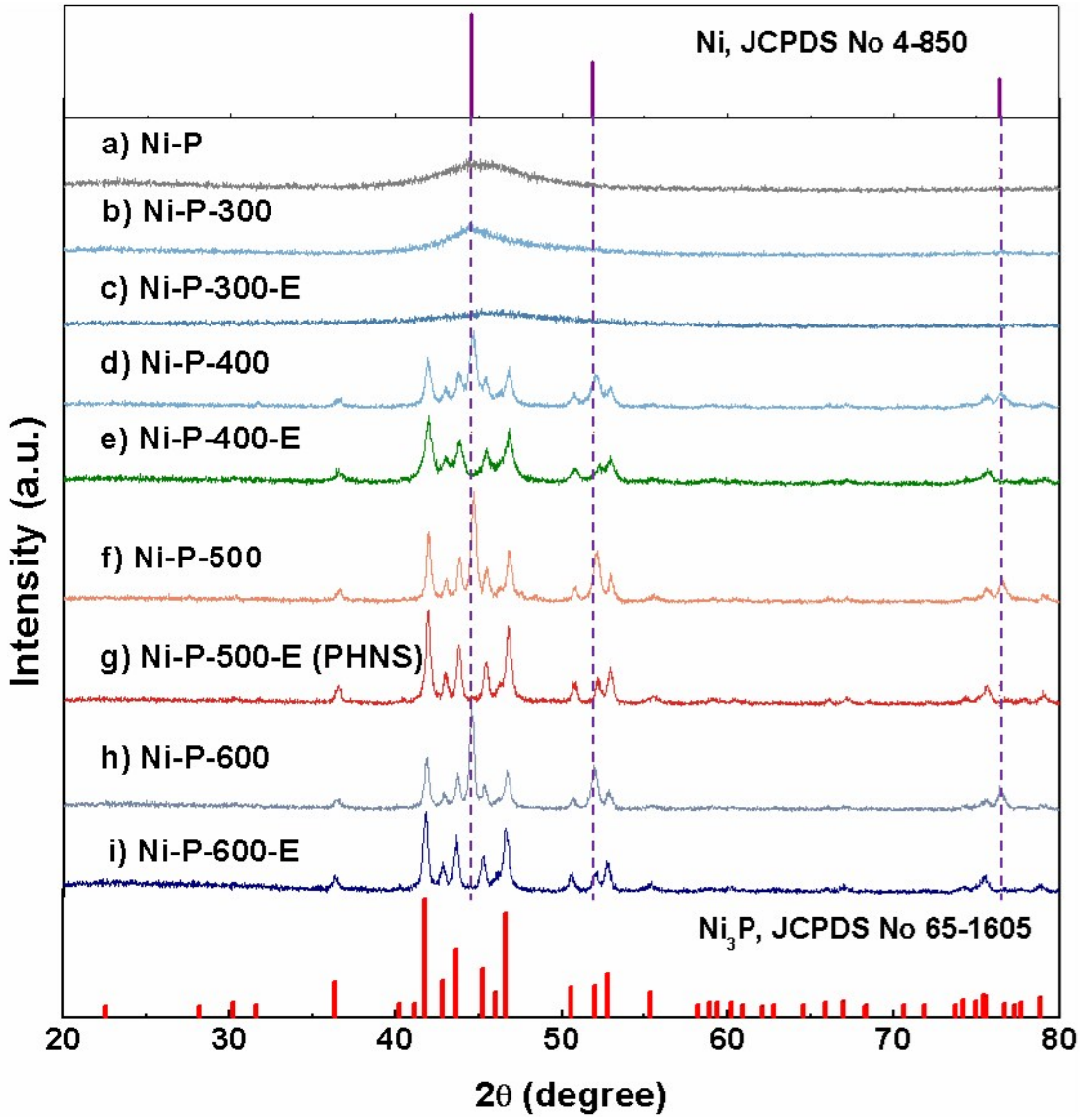

Figure S3. XRD patterns of the samples. With the aid of vertical broken lines it can be seen that the crystalline nickel phase is removed after acidic treatment.

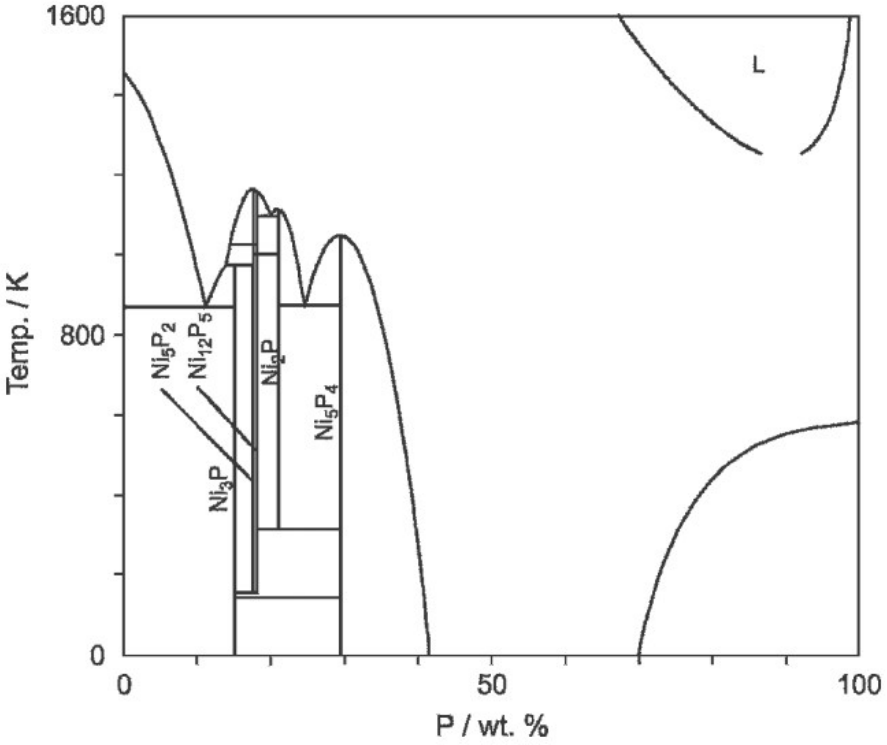

Figure S4. A calculated binary diagram of the Ni-P system.[1]

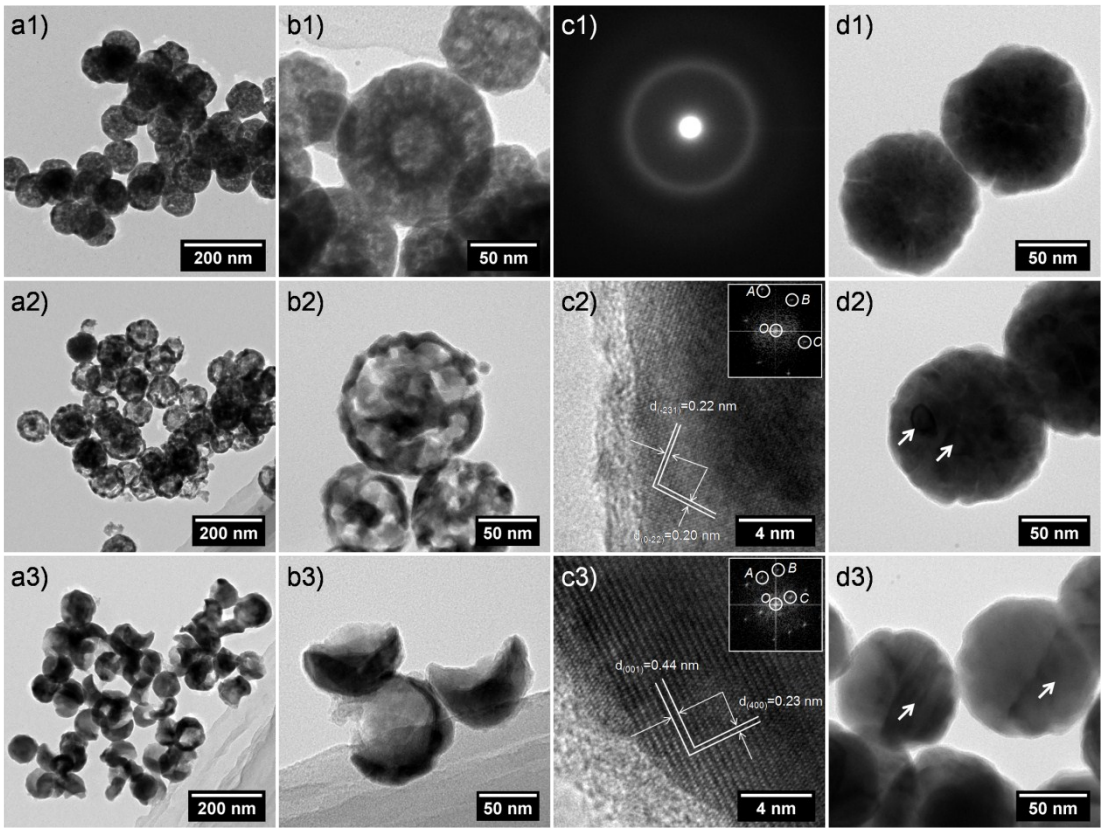

Figure S5. a1) and b1) TEM images of Ni-P-300-E. c1) SAED pattern of Ni-P-300-E. d1) TEM image of Ni-P-300. a2) and b2) TEM images of Ni-P-400-E. c2) HRTEM image of Ni-P-400-E.d2) TEM image of Ni-P-400. a3) and b3) TEM images of Ni-P-600-E. c3) HRTEM image of Ni-P-600-E.d3) TEM image of Ni-P-600. Arrows indicate the darker phase. The SAED patterns in c1) show that Ni-P-300-E is amorphous. The SAED patterns in c2) can be indexed to that of the [-211] zone axis of tetragonal phase Ni_3P (JCPDS No 65-1605). $1/d_{OA} = d_{(2\text{-}51)} = 0.16$ nm, $1/d_{OB} = d_{(0\text{-}22)} = 0.20$ nm, $1/d_{OC} = d_{(-231)} = 0.22$ nm, $\angle AOB = 45^o$, $\angle BOC = 83^o$. The SAED patterns in c3) can be indexed to that of the [010] zone axis of tetragonal phase Ni_3P (JCPDS No 65-1605). $1/d_{OA} = d_{(400)} = 0.23$ nm, $1/d_{OB} = d_{(401)} = 0.20$ nm, $1/d_{OC} = d_{(001)} = 0.44$ nm, $\angle AOB = 27^o$, $\angle BOC = 63^o$.

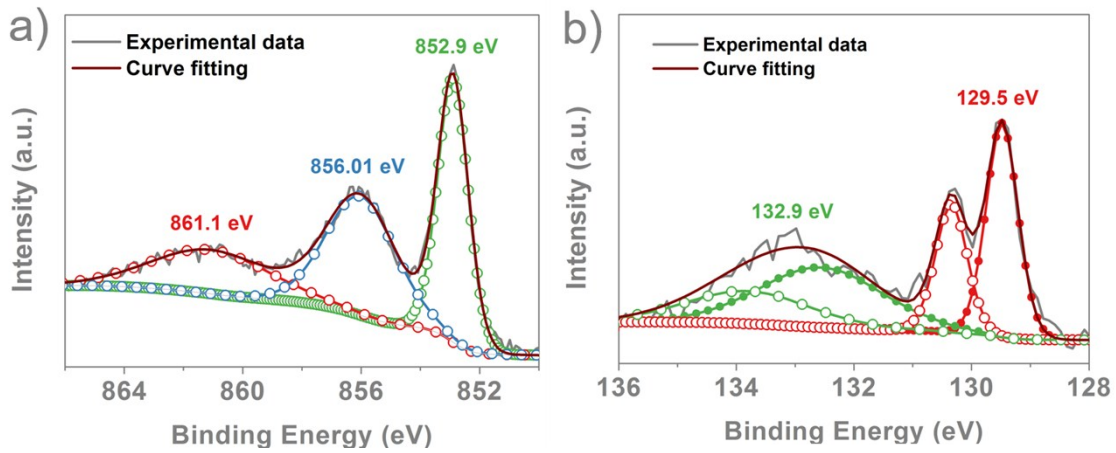

Figure S6. XPS spectra of (a) Ni 2p window and (b) P 2p window. The Ni_3P PHNs were store in vacuum immediately after being freeze dried, and subjected to XPS measurement, avoiding long term air exposure.

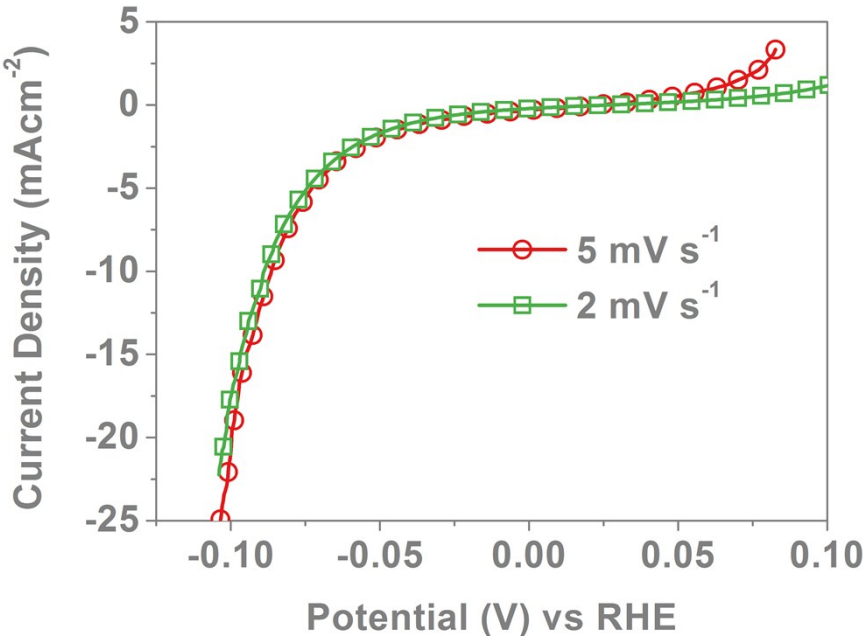

Figure S7. Polarization curve of Ni_3P PHNs measured with the scan rate of 2 and 5 mV s^{-1}.

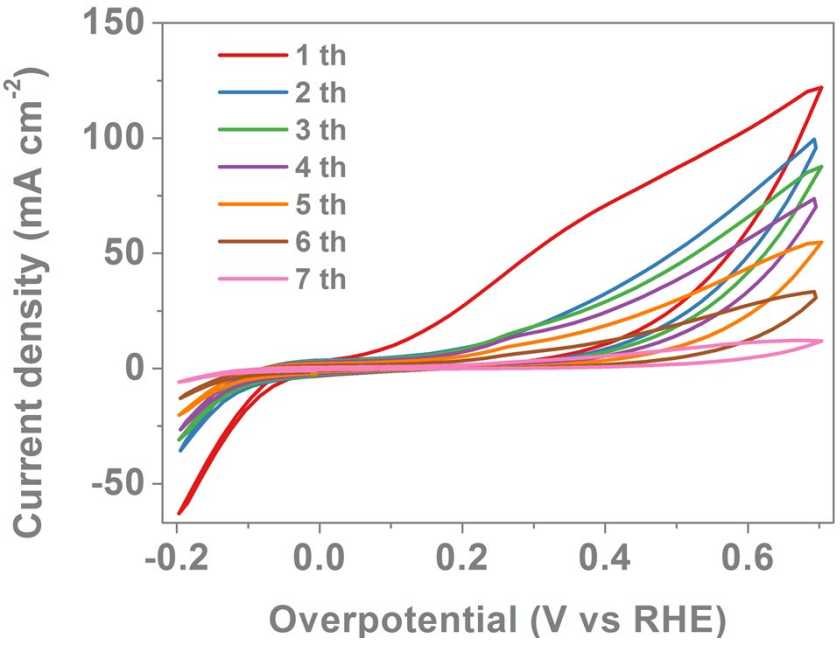

Figure S8. CV scan of Ni_3P PHNs in acidic solution.

Table S1. Summary of HER performance of representative catalysts.

Catalyst	Substrate	Mass density (mg/cm^2)	η_{10}[b] (mV)	η_{20}[c] (mV)	Tafel slope (mV/dec)	J_0[d] (mA/cm^2)	Electrolyte
Ni_2P nanoparticle[2]	Ti foil	1	117	130	$46_{\eta=25-125}$ $81_{\eta=150-200}$	3.3×10^{-2}	0.50 M H_2SO_4
Ni_2P nanoparticle[3]	GCE	0.38		140	87		0.50 M H_2SO_4
$Ni_{12}P_5$ nanoparticle[4]	GCE	3		141			0.50 M H_2SO_4
NiP_2 nanosheet on carbon cloth[5]	Carbon cloth	4.3		99	51	0.26	0.50 M H_2SO_4
CoP nanoparticle[6]	Ti foil	0.9		95	50	1.4×10^{-1}	0.50 M H_2SO_4
CoP nanorod on carbon cloth[7]	carbon cloth	0.92		100	51	2.8×10^{-1}	0.50 M H_2SO_4
CoP particle on carbon nanotube[8]	GCE	0.285	122		54	1.3×10^{-1}	0.50 M H_2SO_4
Co_2P nanorod[9]	GCE	1		167			0.50 M H_2SO_4
FeP nanoparticles[10]	Ti foil	1	50	61	37	4.3×10^{-1}	0.50 M H_2SO_4
FeP nanorods[11]	Ti foil	3.2		72	38	4.2×10^{-1}	0.50 M H_2SO_4
Porous FeP nanosheet[12]	GCE			325	67		
MoP nanoparticle [13]	GCE	0.36	125		54	8.6×10^{-2}	0.50 M H_2SO_4
MoP nanoparticle[14]	GCE			160	54	3.4×10^{-2}	0.50 M H_2SO_4
Cu_3P nanowires on copper foam[15]	copper foam	15.7	143		67	1.8×10^{-1}	0.50 M H_2SO_4
Ni-Mo nanopowder[16]	Ti foil	1		70			2 M NaOH
Ni-Mo nanopowder[16]	Ti foil	3		80			0.5 M H_2SO_4
Ni-Mo nanopowder[16]	Ti foil	1	79	107			1 M NaOH
Bulk Mo_2C[17]	carbon paste electrode	1.4	208	224	$56_{\eta=100-220}$	1.3×10^{-3}	0.50 M H_2SO_4
Bulk MoB[17]	carbon paste electrode	2.5	212	227	$55_{\eta=140-210}$	1.4×10^{-3}	0.50 M H_2SO_4
Mo_2C/CNT[18]	carbon paper	2	149		55.2	1.4×10^{-2}	0.1 M $HClO_4$
Fe-WCN [19]	RRDE	0.4	220		47.1		H_2SO_4(pH 1) + Na_2SO_4 (0.5 M)
Mo_1Soy[20]	carbon paper	1.4	177		66.4	1.3×10^{-2}	0.1 M $HClO_4$
Mo_2C[21]	GCE	0.357	200	210-220	55.8-64.5		0.50 M H_2SO_4
Porous Mo_2C nanowire[22]	GCE	0.21		150	53		0.50 M H_2SO_4
Mo_2C on Gr[23]	GCE	0.285		~160	54		0.50 M H_2SO_4
MoWC nanowire[24]	GCE	1.28		~160	56	3.4×10^{-3}	0.50 M H_2SO_4
Mo_1Soy-RGO[20]	carbon paper	0.47	109		62.7	3.7×10^{-2}	0.1 M $HClO_4$
Mo_2C/C[20]	carbon paper	2	311		87.6	8.1×10^{-3}	0.1 M $HClO_4$
$Co_{0.6}Mo_{1.4}N_2$[25]	GCE	0.243	202	267		2.3×10^{-4}	0.1 M $HClO_4$

MoS_3(33%)/MWCNT-NC[26]	silver electrode	0.255	206	226	$40_{\eta=135-174}$	1.35×10^{-4}	1 M H_2SO_4
Core-shell MoO_3-MoS_2nanowires[27]	FTO		254	272	$50\text{-}60_{\eta=200}$		0.5 M H_2SO_4
Defect-rich MoS_2 nanosheets[28]	GCE	0.285	190	214	$50_{\eta=120-180}$	8.91×10^{-3}	0.5 M H_2SO_4
MoS_2@Au[29]	Au electrode	0.00103	226		69	9.3×10^{-3}	0.5 M H_2SO_4
amorphous MoS_3-CV[30]	GCE		211	229	$40_{\eta=170-200}$	1.3×10^{-4}	1 M H_2SO_4
MoS_2/RGO hybrid[31]	GCE	0.285	154	176	41		0.5 M H_2SO_4
MoS_2/MGF[32]	GCE	0.21	146	159	$42_{\eta=90-120}$		0.5 M H_2SO_4
MoS_2/CNTs[33]	glassy carbon disk	0.136	184	230	44.6		0.5 M H_2SO_4
Cu_2MoS_4[34]	GCE	0.0425	321		95		pH 0 H_2SO_4
WS_2/RGO[35]	GCE	0.4	265	292	58		0.5 M H_2SO_4
WS_2 nanosheets[36]	GCE	0.0001-0.0002 or ca. one continuous layer	233	275	55		0.5 M H_2SO_4
WS_2 nanosheets[37]	GCE	0.285	151	177	72	2.5×10^{-3}	1 M H_2SO_4
Cobalt-sulfide catalyst[38]	FTO		165	227	93		1.0 M pH 7 PBS
$NiWS_x$[39]	FTO		373	430	$96_{\eta=120-150}$	$10^{-2.66}$	pH 7 PBS
$CoWS_x$[39]	FTO		271	311	$78_{\eta=120-150}$	$10^{-2.25}$	pH 7 PBS
$CoMoS_x$[39]	FTO		241	282	$85_{\eta=120-150}$	$10^{-2.89}$	pH 7 PBS
FeS_2[40]	GCE		192.6		62.5	7×10^{-4}	0.5 M H_2SO_4
$FeSe_2$[40]	GCE				65.3	3.5×10^{-4}	0.5 M H_2SO_4
$Fe_{0.43}Co_{0.57}S_2$[40]	GCE		264		55.9	1.3×10^{-3}	0.5 M H_2SO_4
CoS_2[40]	GCE		232		44.6	6.5×10^{-5}	0.5 M H_2SO_4
$CoSe_2$[40]	GCE	0.037	231		42.4	6.5×10^{-5}	0.5 M H_2SO_4
$Co_{0.56}Ni_{0.44}Se_2$[40]	GCE		250		49.7	6.3×10^{-5}	0.5 M H_2SO_4
$Co_{0.32}Ni_{0.68}S_2$[40]	GCE				66.8	3.0×10^{-4}	0.5 M H_2SO_4
NiS_2[40]	GCE				41.6	1.4×10^{-4}	0.5 M H_2SO_4
$NiSe_2$[40]	GCE		250		56.9	5.7×10^{-4}	0.5 M H_2SO_4

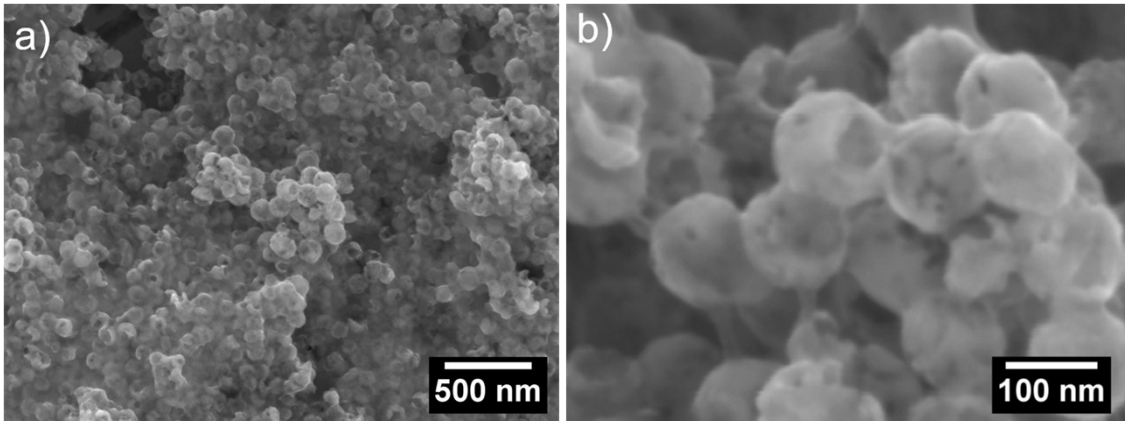

Figure S9. SEM images of Ni3P PHNs subjected to long-term potentiostatic electrolysis in acidic solution.

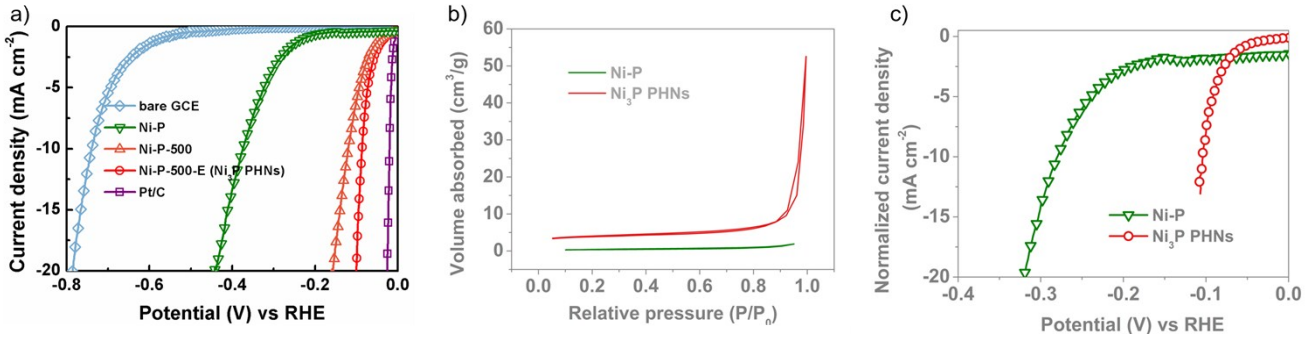

Figure S10. (a) Polarization curves of the intermediates during the formation of Ni_3P PHNs. All potentials were corrected for iR drops. (b) Isotherm plots of Ni-P and Ni_3P PHNs (c) Polarization curves of Ni-P and Ni_3P PHNs normalized from surface area of catalysts.

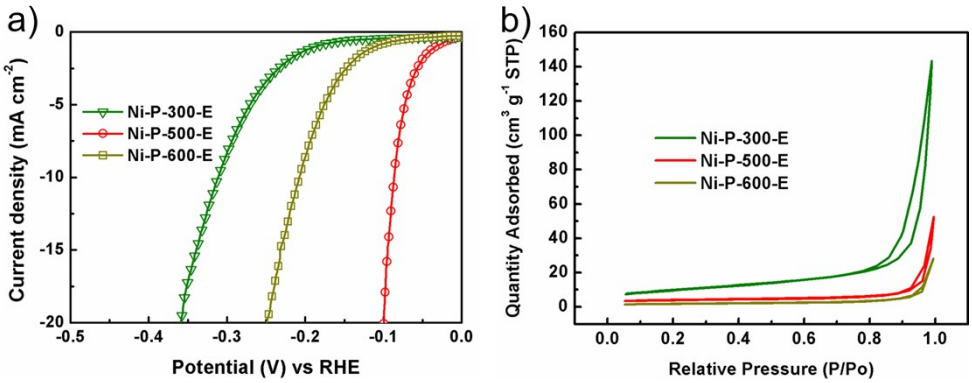

Figure S11. (a) Polarization curves of products corresponding to different annealing temperatures. After annealing, all samples were etched with HCl. All potentials were corrected for iR drops. (b) Isotherm plot of products corresponding to different annealing temperatures.

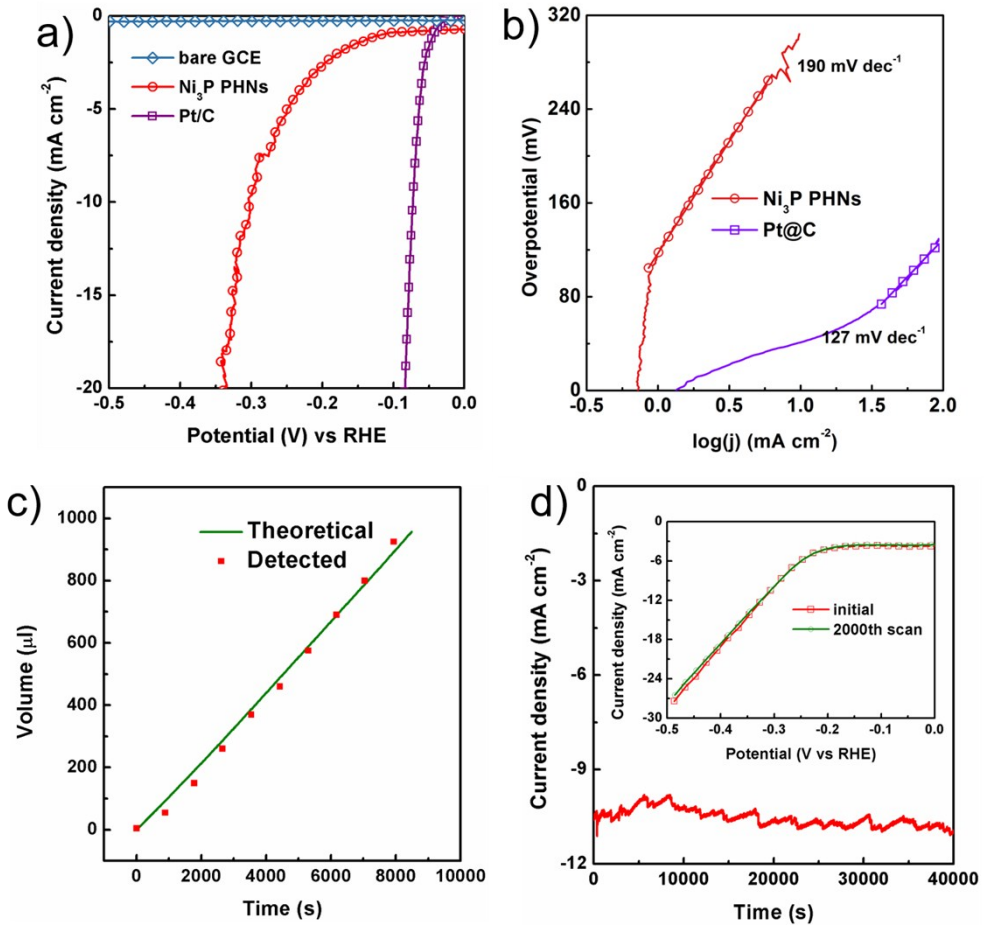

Figure S12. HER performance of the Ni_3P PHNs measured in basic solution (KOH, 1 M). (a) Polarization curves and (b) Tafel plot of the Ni_3P PHNs. (c) Theoretical and detected volumes of hydrogen generated in a potentiostatic electrolysis experiment. (d) Current density of Ni_3P in a potentiostatic electrolysis experiment. The inset of (c) shows the polarization curves corresponding to the initial and 2000th scan in the CV experiments. The polarization curve of Pt/C loaded on GCE is shown for comparison in (a). The loading amounts of the Ni_3P PHNs and Pt/C are both 0.285 mg cm^{-2}. Only the potentials in (a) were corrected for iR drops.

DFT calculations

The electronic properties of Ni_3P were investigated by density functional theory (DFT) calculations using the CASTEP (Cambridge Serial Total Energy Package) package.[41] The wave functions of the valence electrons were expanded in a plane wave basis set with k-vectors within a specified energy cutoff (E_{cut}). Ionic cores were represented by an ultrasoft pseudopotential. Brillouin zone integration was approximated by a sum over special k-points chosen using the Monkhorst-Pack scheme. The exchange correlation contribution to the total electronic energy was treated in a generalized gradient corrected (GGA) approximation, Perdew-Burke-Ernzerhoff functional. The structural parameters were determined using the Broyden-Fletcher-Goldfarb-Shanno (BFGS) minimization technique. The thresholds for the converged structures were set to: energy change less than 1×10^{-5} eV $atom^{-1}$, the maximum residual force less than 0.02 eV $Å^{-1}$, the maximum displacement of atoms less than 0.001 Å, and the maximum stress less than 0.05 GPa. An E_{cut} of 380 eV and a 5×5×3 Monkhorst-Pack k-point mesh ensured convergence of the computed structures and electronic properties in the unit cell optimization,. The calculated lattice parameters of Ni_3P (a = 0.8966 nm, c = 0.4393 nm) are in good agreement with experimental data (a = 0.8954 nm, c = 0.4386 nm).

Utilizing the optimized unit cell described above, a unit cell with a slab of four layers along the (001) direction was applied in the calculation. The slab was repeated periodically with 13 Å vacuum regions between the slabs. A 2×2×1 Monkhorst-Pack k-point mesh was employed, because a larger Monkhorst-Pack k-point mesh (3× 3× 2) induced no significant change in the calculated energies (less than 0.01 eV $cell^{-1}$). Because the slab terminated with a Ni surface has a higher energy than that terminated with a NiP surface, only the slab terminated with the NiP surface was used to model hydrogen adsorption.

The differential adsorption energy of H adsorption was chosen to describe the stability of hydrogen, the equation being given below:

$$\Delta E_H = E(Ni_3P + nH) - E(Ni_3P + (n-1)H) - 1/2E(H_2)$$

where $E(Ni_3P + nH)$ is the total energy of Ni_3P with the n hydrogen atoms adsorbed on the surface, $E(Ni_3P + (n-1)H)$ is the total energy of Ni_3P with (n-1) hydrogen atoms adsorbed on the surface, and $E(H_2)$ is the total energy of a hydrogen molecule in the gas phase.

To evaluate the catalytic activity of Ni_3P, we calculated the Gibbs free energy of hydrogen adsorption as below:

$$\Delta G_H^o = \Delta E_H + \Delta E_{ZPE} - T\Delta S_H$$

where ΔE_{ZPE} is the difference in zero point energy between the adsorbed state and the gas phase and ΔS_H is the entropy difference between the adsorbed state and the gas phase. The overall corrections are taken as:[42, 43]

$$\Delta G_H^o = \Delta E_H + 0.24\ eV$$

The values of ΔG_H^o on the (001) surface of Ni_3P were evaluated from 46 possible adsorption sites of H, which included 8 top sites (Ni1-Ni6, P1-P2: Figure S8a), 24 bridge sites (B1-B24: Figure S8b), and 14 hollow sites (H1-H14: Figure S8c). Twelve structures were obtained after relaxation, which are illustrated in Figure S8d.

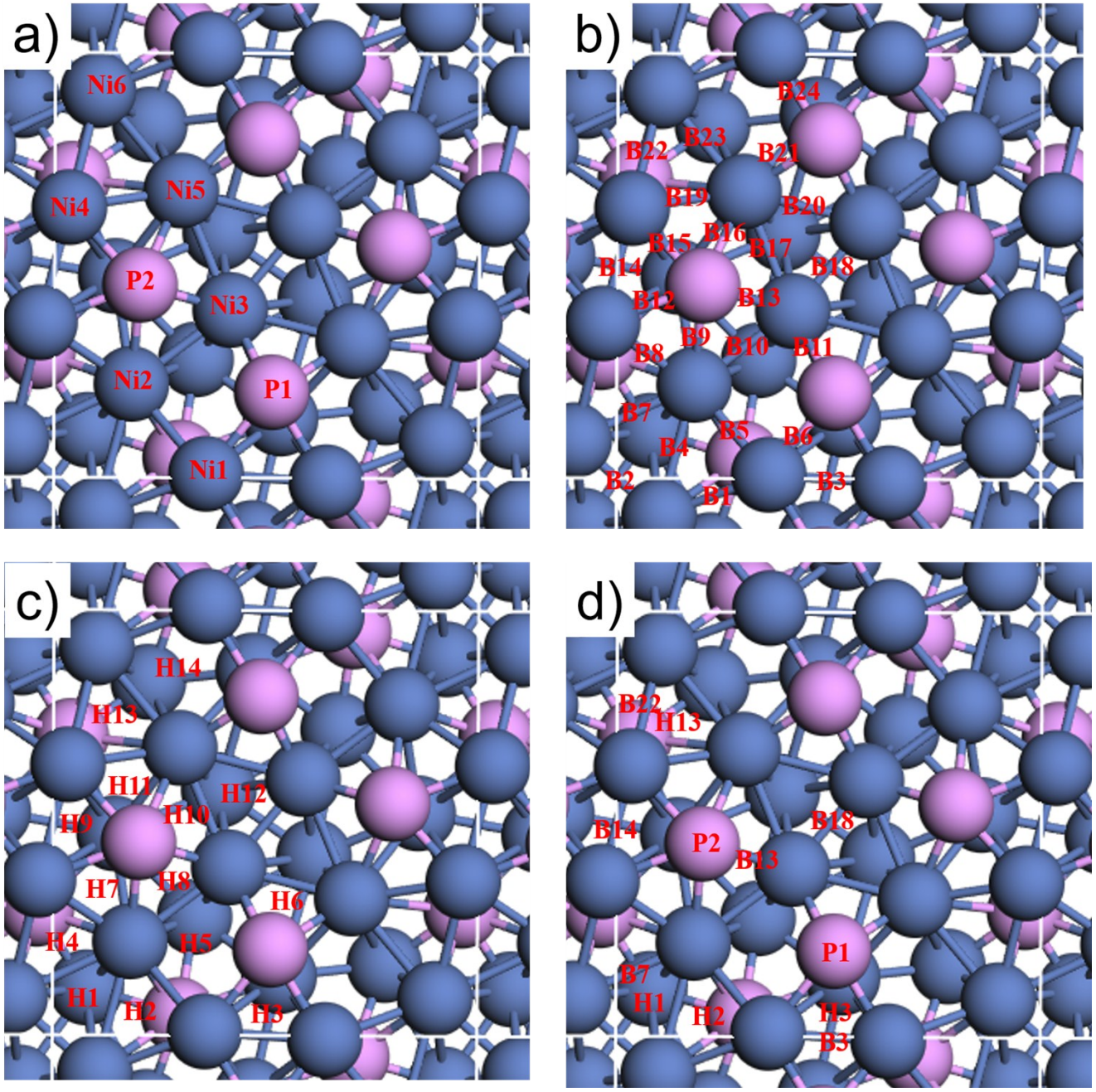

Figure S13. Possible absorption sites on the (001) Ni_3P surface. (a) Top sites, (b) bridge sites, and (c) hollow sites. (d) The absorption sites on the (001) Ni_3P surface suggested by a geometry optimization. The white square depicts a unit cell on the (001) Ni_3P surface. (: Ni; :P)

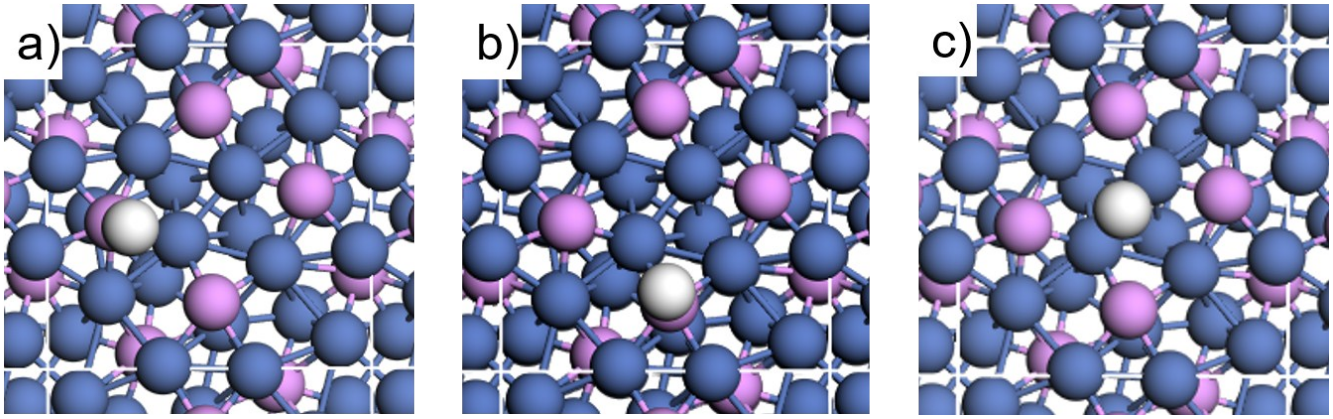

Figure S14. Configuration of hydrogen absorbed at (a) P2, (b) P1, and (c) B18 sites. The white squares depict unit cells on the (001) Ni_3P surface. (: Ni; : P; : H)

References

1. M. Murayama, A. Belyakov, T. Hara, Y. Sakai, K. Tsuzaki, M. Okubo, M. Eto and T. Kimura, *J. Electron. Mater.*, 2006, **35**, 1787-1792.
2. E. J. Popczun, J. R. McKone, C. G. Read, A. J. Biacchi, A. M. Wiltrout, N. S. Lewis and R. E. Schaak, *J. Am. Chem. Soc.*, 2013, **135**, 9267-9270.
3. L. G. Feng, H. Vrubel, M. Bensimon and X. L. Hu, *Phys. Chemi. Chem. Phys.*, 2014, **16**, 5917-5921.
4. Z. P. Huang, Z. B. Chen, Z. Z. Chen, C. C. Lv, H. Meng and C. Zhang, *ACS Nano*, 2014, **8**, 8121-8129.
5. P. Jiang, Q. Liu and X. P. Sun, *Nanoscale*, 2014, **6**, 13440-13445.
6. E. J. Popczun, C. G. Read, C. W. Roske, N. S. Lewis and R. E. Schaak, *Angew. Chem. Int. Ed.*, 2014, **53**, 5427-5430.
7. J. Q. Tian, Q. Liu, A. M. Asiri and X. P. Sun, *J. Am. Chem. Soc.*, 2014, **136**, 7587-7590.
8. Q. Liu, J. Q. Tian, W. Cui, P. Jiang, N. Y. Cheng, A. M. Asiri and X. P. Sun, *Angew. Chem. Int. Ed.*, 2014, **53**, 6710-6714.
9. Z. P. Huang, Z. Z. Chen, Z. B. Chen, C. C. Lv, M. G. Humphrey and C. Zhang, *Nano Energy*, 2014, **9**, 373-382.
10. J. F. Callejas, J. M. McEnaney, C. G. Read, J. C. Crompton, A. J. Biacchi, E. J. Popczun, T. R. Gordon, N. S. Lewis and R. E. Schaak, *ACS Nano*, 2014, **8**, 11101-11107.
11. P. Jiang, Q. Liu, Y. H. Liang, J. Q. Tian, A. M. Asiri and X. P. Sun, *Angew. Chem. Int. Ed.*, 2014, **53**, 12855-12859.
12. Y. Xu, R. Wu, J. F. Zhang, Y. M. Shi and B. Zhang, *Chem. Commun.*, 2013, **49**, 3.
13. Z. C. Xing, Q. Liu, A. M. Asiri and X. P. Sun, *Adv. Mater.* , 2014, **26**, 5702-5707.
14. P. Xiao, M. A. Sk, L. Thia, X. M. Ge, R. J. Lim, J. Y. Wang, K. H. Lim and X. Wang, *Energ. Environ. Sci.*, 2014, **7**, 2624-2629.
15. J. Q. Tian, Q. Liu, N. Y. Cheng, A. M. Asiri and X. P. Sun, *Angew. Chem. Int. Ed.*, 2014, **53**, 9577-9581.
16. J. R. McKone, B. F. Sadtler, C. A. Werlang, N. S. Lewis and H. B. Gray, *ACS Catal.*, 2013, **3**, 166-169.
17. H. Vrubel and X. L. Hu, *Angew. Chem. Int. Ed.*, 2012, **51**, 12703-12706.
18. W. F. Chen, C. H. Wang, K. Sasaki, N. Marinkovic, W. Xu, J. T. Muckerman, Y. Zhu and R. R. Adzic, *Energ. Environ. Sci.*, 2013, **6**, 943-951.
19. Y. Zhao, K. Kamiya, K. Hashimoto and S. Nakanishi, *Angew. Chem. Int. Ed.*, 2013, **52**, 1-5.
20. W. F. Chen, S. Iyer, S. Iyer, K. Sasaki, C. H. Wang, Y. M. Zhu, J. T. Muckerman and E. Fujita, *Energ. Environ. Sci.*, 2013, **6**, 1818-1826.
21. C. J. Ge, P. Jiang, W. Cui, Z. H. Pu, Z. C. Xing, A. M. Asiri, A. Y. Obaid, X. P. Sun and J. Tian, *Electrochim Acta*, 2014, **134**, 182-186.
22. L. Liao, S. N. Wang, J. J. Xiao, X. J. Bian, Y. H. Zhang, M. D. Scanlon, X. L. Hu, Y. Tang, B. H. Liu and H. H. Girault, *Energ. Environ. Sci.*, 2014, **7**, 387.
23. L. F. Pan, Y. H. Li, S. Yang, P. F. Liu, M. Q. Yu and H. G. Yang, *Chem. Commun.*, 2014, **50**, 13135-13137.
24. P. Xiao, X. M. Ge, H. B. Wang, Z. L. Liu, A. Fisher and X. Wang, *Adv. Funct. Mater.*, 2015, **25**, 1520-1526.

25. B. F. Cao, C. M. Veith, J. C. Neuefeind, R. R. Adzic and P. G. Khalifah, *J. Am. Chem. Soc.*, 2013, **135**, 19186-19192.
26. T. W. Lin, C. J. Liu and J. Y. Lin, *Appl. Catal. B- Environ.*, 2013, **134-135**, 75-82.
27. Z. Chen, D. Cummins, B. N. Reinecke, E. Clark, M. K. Sunkara and T. F. Jaramillo, *Nano. Lett.*, 2011, **11**, 4168-4175.
28. J. Xie, H. Zhang, S. Li, R. Wang, X. Sun, M. Zhou, J. Zhou, X. W. Lou and Y. Xie, *Adv. Mater.*, 2013, **25**, 5807-5813.
29. T. Y. Wang, L. Liu, Z. W. Zhu, P. Papakonstantinou, J. B. Hu and M. Li, *Energ. Environ. Sci.*, 2013, **6**, 625-633.
30. D. Merki, S. Fierro, H. Vrubel and X. L. Hu, *Chem. Sci.*, 2011, **2**, 1262-1267.
31. Y. Li, H. Wang, L. Xie, Y. Liang, G. Hong and H. Dai, *J. Am. Chem. Soc.*, 2011, **133**, 7296-7299.
32. L. Liao, J. Zhu, X. J. Bian, L. N. Zhu, M. D. Scanlon, H. H. Girault and B. H. Liu, *Adv. Funct. Mater.*, 2013, **23**, 5326-5333.
33. Y. Yan, X. Ge, Z. Liu, J. Y. Wang, J. M. Lee and X. Wang, *Nanoscale*, 2013, **5**, 7768-7771.
34. P. D. Tran, M. Nguyen, S. S. Pramana, A. Bhattacharjee, S. Y. Chiam, J. Fize, M. J. Field, V. Artero, L. H. Wong, J. Loo and J. Barber, *Energ. Environ. Sci.*, 2012, **5**, 8912-8916.
35. J. Yang, D. Voiry, S. J. Ahn, D. Kang, A. Y. Kim, M. Chhowalla and H. S. Shin, *Angew. Chem. Int. Ed.*, 2013, **52**, 13751-13754.
36. D. Voiry, H. Yamaguchi, J. Li, R. Silva, D. C. Alves, T. Fujita, M. Chen, T. Asefa, V. B. Shenoy, G. Eda and M. Chhowalla, *Nature Mater.*, 2013, **12**, 850-855.
37. Z. Z. Wu, B. Z. Fang, B. Arman, A. K. Sun, D. P. Wilkinson and D. Z. Wang, *Appl. Catal. B-Environ.*, 2012, **125**, 59-66.
38. Y. Sun, C. Liu, D. C. Grauer, J. Yano, J. R. Long, P. Yang and C. J. Chang, *J. Am. Chem. Soc.*, 2013, **135**, 17699-17702.
39. P. D. Tran, S. Y. Chiam, P. P. Boix, Y. Ren, S. S. Pramana, J. Fize, V. Artero and J. Barber, *Energ. Environ. Sci.*, 2013, **6**, 2452-2459.
40. D. S. Kong, J. J. Cha, H. T. Wang, H. R. Lee and Y. Cui, *Energ. Environ. Sci.*, 2013, **6**, 3553-3558.
41. S. J. Clark, M. D. Segall, C. J. Pickard, P. J. Hasnip, M. J. Probert, K. Refson and M. C. Payne, *Zeitschrift fuer Kristallographie*, 2005, **220**, 567-570.
42. J. K. Nørskov, T. Bligaard, A. Logadottir, J. R. Kitchin, J. G. Chen, S. Pandelov and U. Stimming, *J. Electrochem. Soc.*, 2005, **152**, J23-J26.
43. Y. Zheng, Y. Jiao, Y. H. Zhu, L. H. Li, Y. Han, Y. Chen, A. J. Du, M. Jaroniec and S. Z. Qiao, *Nature Commun.*, 2014, **5**, 3783.